

# A Radial Time Projection Chamber for $\alpha$ detection in CLAS at JLab

R. Dupré<sup>a,b,\*</sup>, S. Stepanyan<sup>c</sup>, M. Hattawy<sup>a,b</sup>, N. Baltzell<sup>a,c</sup>, K. Hafidi<sup>a</sup>, M. Battaglieri<sup>d</sup>, S. Bueltmann<sup>e</sup>, A. Celentano<sup>d</sup>, R. De Vita<sup>d</sup>, A. El Alaoui<sup>a,f</sup>, L. El Fassi<sup>g</sup>, H. Fenker<sup>c</sup>, K. Kosheleva<sup>a</sup>, S. Kuhn<sup>e</sup>, P. Musico<sup>d</sup>, S. Minutoli<sup>d</sup>, M. Oliver<sup>h</sup>, Y. Perrin<sup>i</sup>, B. Torayev<sup>e</sup>, E. Voutier<sup>b,i</sup>

<sup>a</sup>Argonne National Laboratory, Argonne IL 60439, USA

<sup>b</sup>Institut de Physique Nucléaire, CNRS/IN2P3 and Université Paris Sud, Orsay, France

<sup>c</sup>Jefferson Laboratory, Newport News, VA 230606, USA

<sup>d</sup>INFN, Sezione di Genova, 16146 Genova, Italy

<sup>e</sup>Old Dominion University, Norfolk, VA 23529, United States

<sup>f</sup>Universidad Técnica Federico Santa María, Casilla 110-V Valparaíso, Chile

<sup>g</sup>Mississippi State University, Mississippi State, MS 39762-5167

<sup>h</sup>University of Chicago, Chicago, IL 60637, United States

<sup>i</sup>LPSC, Université Grenoble-Alpes, CNRS/IN2P3, Grenoble, France

## Abstract

A new Radial Time Projection Chamber (RTPC) was developed at the Jefferson Laboratory to track low-energy nuclear recoils to measure exclusive nuclear reactions, such as coherent deeply virtual Compton scattering and coherent meson production off  $^4\text{He}$ . In 2009, we carried out these measurements using the CEBAF Large Acceptance Spectrometer (CLAS) supplemented by the RTPC positioned directly around a gaseous  $^4\text{He}$  target, allowing a detection threshold as low as 12 MeV for  $^4\text{He}$ . This article discusses the design, principle of operation, calibration methods and performances of this RTPC.

**Keywords:** Time projection chamber, gas electron multipliers, alpha particles, DVCS, Nuclear physics

## 1. Introduction

Until recently, the Thomas Jefferson National Accelerator Facility, in Newport News, Virginia, USA, has provided high power electron beams of up to 6 GeV energy and 100% duty factor to three experimental Halls (A, B, C) simultaneously. The CLAS spectrometer [1], located in Hall-B, was based on a superconducting toroidal magnet and composed of several sub-detectors. Figure 1 shows a three dimensional representation of the baseline CLAS spectrometer:

- Three regions of Drift Chambers (DC) for the tracking of charged particles [2].
- Superconducting toroidal magnet to bend the trajectories of charged particles, thus allowing momentum measurement with the DC tracking information.
- Threshold Cherenkov Counters (CC) for electron identification at momenta  $< 2.7 \text{ GeV}/c$  [3].
- Scintillation Counters (SC) to identify charged hadrons by measuring their time of flight [4].
- Electromagnetic Calorimeters (EC) for identification of electrons, photons and neutrons [5].

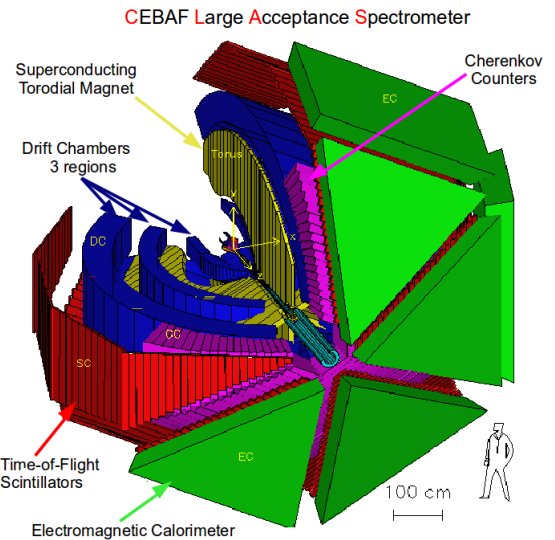


Figure 1: A three dimensional representation of the baseline CLAS setup. The full description is given in the text.

For certain experiments the base CLAS system was complimented with ancillary detectors. For example, the measurement of the Deeply Virtual Compton Scattering (DVCS) process ( $eH \rightarrow e'H'\gamma$ , where  $H$  is a nucleon or nucleus) necessitates an upgrade of the photon detection system. Indeed, with a 6 GeV electron beam, the majority of DVCS photons are produced at very forward angles, where the acceptance of the EC was poor. To extend the detection range, an inner calorimeter (IC) was built for the E01-113 experiment in 2005 [6]. The IC was constructed from 424 lead-tungstate ( $\text{PbWO}_4$ ) crystals, covering polar angles between  $5^\circ$  and  $15^\circ$  [7]. To protect the CLAS detector and the IC from the large flux of low energy Møller electrons, a 5 T solenoid magnet was placed around the target to shield the detectors. To detect recoiling  $\alpha$  particles from the coherent DVCS on Helium, a new radial time projection chamber (RTPC) was developed to track low energy nuclear fragments. The solenoid field was used to bend tracks and measure momentum of particles in the RTPC. The CLAS detector supplemented with both IC and RTPC was used during a three months experimental run [8, 9] in 2009 with a longitudinally polarized electron beam of 130 nA and energy of 6.064 GeV incident on a gaseous  $^4\text{He}$  target.

The original design of the RTPC was developed for the BoNuS experiment at Jefferson Lab which took data with CLAS in 2005 [10]. Significant improvements were made to the RTPC mechanical structure and fabrication technique that both increased the acceptance and reduced the amount of material in the path of the outgoing particles. The enhanced design, used in the 2009 DVCS experiment, is described in section 2 of this paper. The data acquisition system described in section 3 was reconfigured to increase the event readout rate. The calibration methods are discussed in section 4 and the tracking algorithm in section 5. Finally, the overall performance of the RTPC is described in section 6.

## 2. RTPC design

With a 6 GeV incident electron energy, the recoiling  $^4\text{He}$  nuclei from coherent DVCS have an average momentum around 300 MeV/c (12 MeV kinetic energy). Such low energy  $\alpha$  particles are stopped very rapidly, so the RTPC was designed to be as close as possible to the target and fit inside the 230 mm diameter shell and cryostat wall of the solenoid magnet bore.

The new CLAS RTPC is a 250 mm long cylinder of 158 mm diameter, leaving just enough room to fit pre-amplifiers between the RTPC outer shell and the solenoid. The electric field is directed perpendicularly to the beam direction, such that drifting electrons are pushed away from the beam line. These electrons are amplified by three

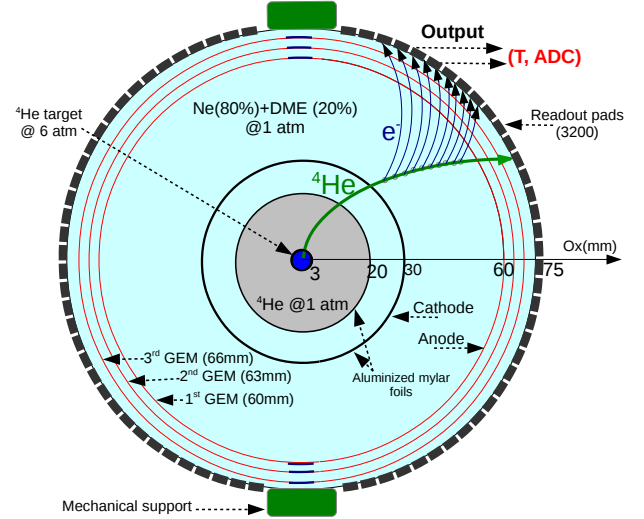


Figure 2: Schematic drawing of the CLAS RTPC in a plane perpendicular to the beam direction. See text for description of the elements.

layers of semi-cylindrical gas electron multipliers (GEM) [11] and detected by the readout system on the external shell of the detector as illustrated in Figure 2. The RTPC is segmented into two halves with independent GEM amplification systems that cover about 80% of the azimuthal angle.

We detail here the different regions shown in Figure 2 starting from the beam line towards larger radius:

- The 6 atm  $^4\text{He}$  target extends along the beamline forming the detector central axis; it is a 292 mm long, 6 mm diameter Kapton straw with a  $27 \mu\text{m}$  wall. The detector and the target are centered at 64 cm to the left of CLAS's center.
- The first gas gap covers the radial range from 3 mm to 20 mm. It is filled with  $^4\text{He}$  gas at 1 atm to minimize secondary interactions from Møller electrons scattered by the beam. This region is surrounded by a  $4 \mu\text{m}$  thick window made of grounded aluminized Mylar.
- The second gas gap region extends between 20 mm and 30 mm and is filled with the gas mixture of 80% neon (Ne) and 20% dimethyl ether (DME). This region is surrounded by a  $4 \mu\text{m}$  thick window made of aluminized Mylar set at  $-4260 \text{ V}$  to serve as the cathode.
- The drift region is filled with the same Ne-DME gas mixture and extends from the cathode to the first GEM, 60 mm away from the beam axis. The average electric field in this region is perpendicular to the beam and about  $550 \text{ V/cm}$ .
- The electron amplification system is composed of three GEMs located at radii of 60, 63 and 66 mm. In

\*Corresponding author

Email address: dupre@ipno.in2p3.fr (R. Dupré)

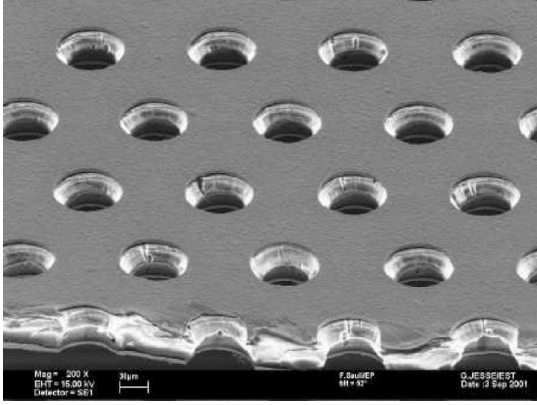


Figure 3: Image of a typical GEM foil similar to the one used for our RTPC [11].

this configuration, the first GEM layer serves as the anode and each subsequent GEM is set at a lower voltage to obtain a strong ( $\sim 1600$  V/cm) electric field between the GEM foils. A 275 V bias is applied across each GEM for amplification.

- The readout board has an internal radius of 69 mm and collects charges after they have been multiplied by the GEMs. Pre-amplifiers are plugged directly on its outer side and transmit the signal to the data acquisition electronics.

The GEM technology has been chosen for the flexibility of the GEM foils, which can be easily used to produce a curved amplification surface. Also, GEMs are known to have relatively low spark rate [12], which is important when trying to detect highly ionizing slow nuclei that deposit large amount of energy. The GEMs for this RTPC are made from a Kapton insulator layer,  $50\ \mu\text{m}$  thick, sandwiched between two  $5\ \mu\text{m}$  copper layers<sup>1</sup>. The mesh of each GEM layer is chemically etched with  $50\ \mu\text{m}$  diameter holes with double-conical shapes as illustrated in Figure 3. The potential difference applied between the two copper layers of the GEM creates a very strong electric field in each hole leading to high ionization and amplification.

The drift gas used in the experiment is a 80-20% Ne-DME mixture. This choice has been made in order to balance the energy deposit, which is critical for proper particle identification, with a reasonable Lorentz angle. Calculations using the MAGBOLTZ program [13] showed that with the 5 T solenoidal magnetic field, we would have a Lorentz angle of about  $23^\circ$  with this gas mixture.

One of the important challenges in developing the RTPC was to obtain a good support structure for the GEM foils to allow a tractable installation of the GEMs. At the same time, we wanted to keep the material budget small in the forward region where we detect other particles in subsequent detectors. We successfully realized these prerequisites by using fiber glass rings glued to each end of the

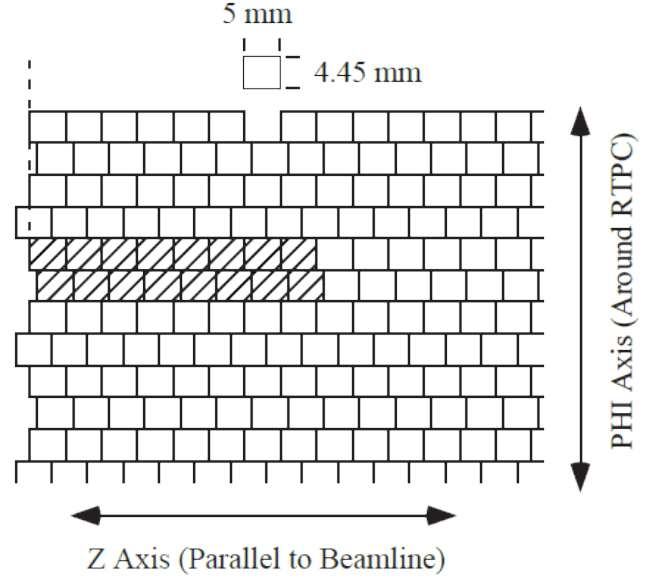


Figure 4: A schematic representation of the readout pads. The shaded sixteen pads are a group of pads that are connected to the same pre-amplifier.

GEM foils to form self supporting cylinders that could be installed independently in the RTPC after gluing and soldering operations. The rigidity of the GEM foils was enough for the structure to be self-supporting and only the upstream end of the cylinder was fixed to the main mechanical support structure. This design only left a light fiberglass ring in the downstream end, reducing to a minimum secondary interactions.

### 3. Readout System

The RTPC electron collection system had 3200 readout pads. These elements were located at the end of the amplification region, 69 mm from the central axis. Figure 4 illustrates the configuration of the 5 by 4.45 mm pads, where the shift between the rows was implemented to reduce aliasing. Each half of the RTPC had 40 rows and 40 columns of pads. The shaded region in Figure 4 shows how pads were grouped to 16 channels pre-amplifier boards. The pre-amplifier boards, already employed in the BoNuS RTPC [10], serve the dual purpose of inverting the RTPC signals polarity – from negative to positive – to match the requirements of the subsequent readout system, and driving the 6 m long ribbon cable that connects to it.

The readout system, similar to the original BoNuS RTPC system [10], was based on the front end electronic boards originally developed for the ALICE TPC readout system at CERN [14]. The Front End Card (FEC) hosted the analogue receiver circuit and the subsequent amplification and digitization stages, based on the PASA [15] and ALTRO [16] ASICS. A Readout Control Unit (RCU) board was used to distribute the trigger signal to FECs and for data readout, with each RCU handling up to 25

<sup>1</sup>The GEM foils were produced by Tech-Etch, Inc.

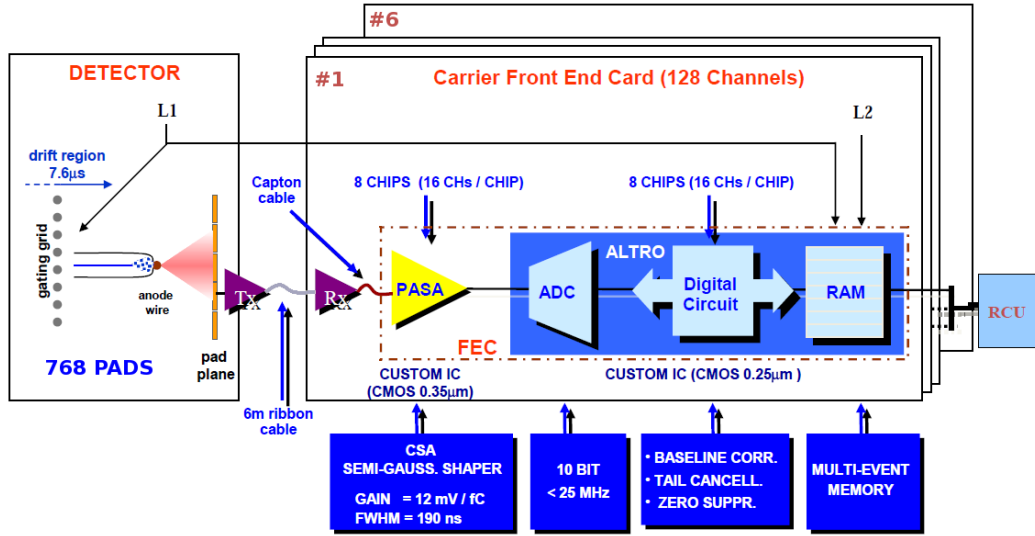


Figure 5: Schematic representation of the RTPC readout system, showing the different elements of the front end electronics.

FECs. Communication between readout controller appli-207 cation (ROC) and FECs was performed trough a custom208 backplane, implementing a low-voltage signal bus. The209 RCU communicated with the CLAS DAQ system trough210 a 200 MB/s optical link, connected to a data acquisition211 PC hosting a readout receiver card. This PC hosted the212 ROC used to interface with the CLAS DAQ system. An213 Ethernet link was also present, for slow-controls and mon-214 itoring.

The standard CLAS electron trigger was used to initi-216 ate the RTPC readout. For each event, 100 samples/channel217 were digitized and processed by the ALTRO ASIC. In218 order to reduce the data size, ALTRO was operated in219 zero-suppression mode, keeping only samples from chan-220 nels above a programmable threshold set just above the noise level. Samples were pre-processed by a glitch-filter to221 reject noise and spurious pulses. To properly reconstruct222 the signal shape,  $N_{PRE} = 3$  samples before threshold-223 crossing and  $N_{POST} = 3$  samples after the signal returns224 below threshold were saved.

The trigger signal also initiates RCU readout operation225 from FEC boards. All the measured samples from active226 channels are reported, together with a channel identifier227 and a timestamp, to the ROC application, that in turns228 sends them on the main event builder. Readout from FECs229 occurs in “block-transfer” mode, making use of the AL-230 TRO internal multi-event buffer. This feature could be231 exploited thanks to the new RCU boards developed for the232 RTPC readout system<sup>2</sup>. In order to read all the detector233 readout pads, four FEC crates were used, each equipped234 with 6 boards, plus a ROC. A schematic of the readout235

system, for a single crate, is reported in Figure 5. This configuration permitted to reduce the dead time associ-207 ated to FEC readout operations, which is scaling linearly208 with the number of boards in the crate. During the 2009209 run, the system was successfully operated with a DAQ rate210 of 3.1 kHz and a live time of 70%, for a luminosity of about211  $10^{34} \text{ cm}^{-2} \cdot \text{s}^{-1}$  and a beam energy of 6.064 GeV.

Finally, during data reconstruction, the acquired sam-212 ples were processed to obtain, for each readout pad, the213 accumulated charge (ADC) and the pulse time (T). Since214 pulse time was obtained as the time-stamp of the first sam-215 ple above threshold, referred to the trigger time, the reso-216 lution is equivalent to the ALTRO sampling time, 100 ns.

#### 4. Calibration

The timing information collected for each signal above226 threshold was used to infer the origin of the ionization elec-227 trons and then the trajectory of the detected particle. The228 recorded ADCs were used to reconstruct the deposited en-229 ergy per unit of length ( $\frac{dE}{dX}$ ) which, together with the mo-230 mentum calculated from the trajectory, enabled the particle231 identification.

In this section we will detail the methods used to cal-232 ibrate the drift speed, drift paths and gains of the detec-233 tor. Drift speed and paths were initially calculated using234 the MAGBOLTZ [13] program, then refined using data235 to account for variations of the run conditions. We al-236 ways assume cylindrical symmetry in the chamber for the237 calibration, such that none of the parameters depend on238 the azimuthal angle  $\phi$ . The initial MAGBOLTZ calibra-239 tion was improved through several iterations of the process240 described below, with each time an increasing number of241 tracks reconstructed in the RTPC. The figures presented242 in this section are the ones obtained while performing the243 last iteration of this calibration process.

<sup>2</sup>In the original BoNuS system, the U2F readout controller had237 no multi-event capability and used a USB connection rather than238 fiber optics for readout. These factors limited the maximum readout239 rate from the BoNuS detector to about 500 Hz.240



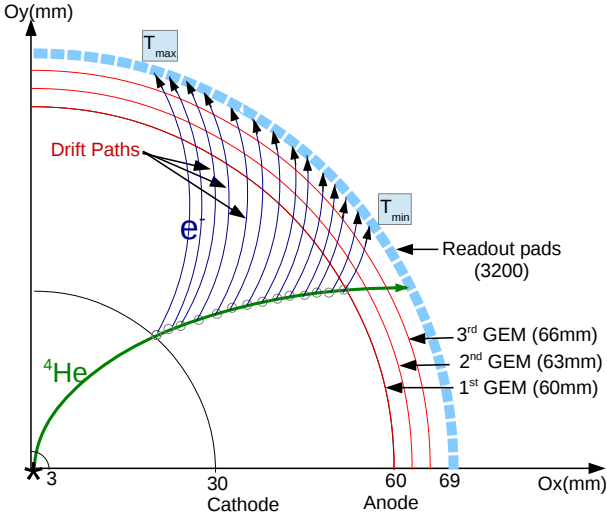


Figure 6: A schematic drawing of a  $^4\text{He}$  track (in green) traversing the drift region, with the drift paths followed by the electrons (in black).

#### 4.1. Drift Speed Parametrization

After the ionization, the released electrons drift to the cylindrical detection plane under the effect of the electric field. The electrons released close to the cathode take the most time to reach the readout pads, the cylindrical symmetry insures that this maximum drift distance is the same for all tracks. We illustrate this in Figure 6, where we depict a typical  $^4\text{He}$  track. By measuring the maximum time ( $T_{Max}$ ), we can therefore infer the drift speed of the electrons in the RTPC.

To measure the maximum drift time, we used the time profile of hits from identified tracks shown in Figure 7. We can clearly observe the dropping edge expected from geometrical considerations. We define a value  $T_{Max/2}$  at which the dropping edge passes half the maximum number of hits in the histogram. This value was measured in bins along the 200 mm RTPC's length to take into account variations in the electric and magnetic field in the RTPC (see Figure 8).

Due to the non perfect experimental conditions, in particular possible contamination of our gas mixture, the drift speed changed during the three months long experimental run<sup>3</sup>. Figure 9 shows the  $T_{Max/2}$  values for individual runs (approximately 2 hours long). We observe significant change in the drift speed before and after run 61600, while variations within these periods are around 2%.

In summary, we obtain from our calibration a parametrization of the drift speed as a function of both position along

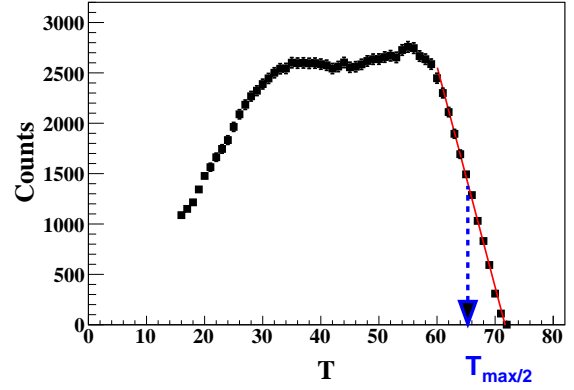


Figure 7: Time distribution of the hits associated with a track in one experimental run. Trigger time is defined as  $T=15$ , the time unit is the ALTRO sampling time of 100 ns.

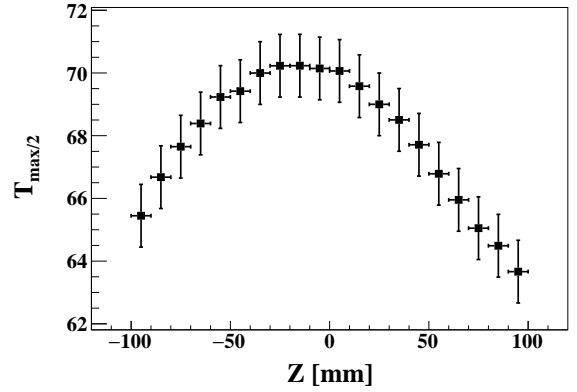


Figure 8: Maximum time of collected hits as a function of the track position on the  $z$ -axis for one experimental run.

the beam axis and the run number. These functions were extracted for our entire data set and implemented in the track reconstruction code.

#### 4.2. Drift Path Calibration

The drift path is the trajectory followed by the electrons released through ionization in the gas. We calculated them with MAGBOLTZ [13], but it requires knowledge of the detector's geometry, gas mixture composition, and of course the electric and magnetic fields over the whole volume of the detector. We used this calculation as a first calibration, but, as can be seen with the drift speed, conditions in the chamber were changing over time. Moreover, the  $4\text{ }\mu\text{m}$  foil used as a cathode is easily deformed, such that we expect the geometrical accuracy to be of few millimeters, directly impacting our knowledge of the electric field. These problems, already encountered for the BoNuS RTPC calibration [10], motivated the acquisition of specific calibration runs. These were taken with a lower energy electron beam (1.204 and 1.269 GeV) to enhance the cross section of the elastic scattering ( $e^4\text{He} \rightarrow e^4\text{He}$ ). In this process, the measurement of the electron kinematics allows to calculate directly the kinematics of the He-

<sup>3</sup>We had to increase the gas flow during the experiment due to a small leak in the RTPC, which concurred to the large shift of drift time observed around run number 61600. While our gas system was kept slightly over atmospheric pressure to limit contamination from air or other external gases, it is likely that this leak was the source of modification of the drift speed.

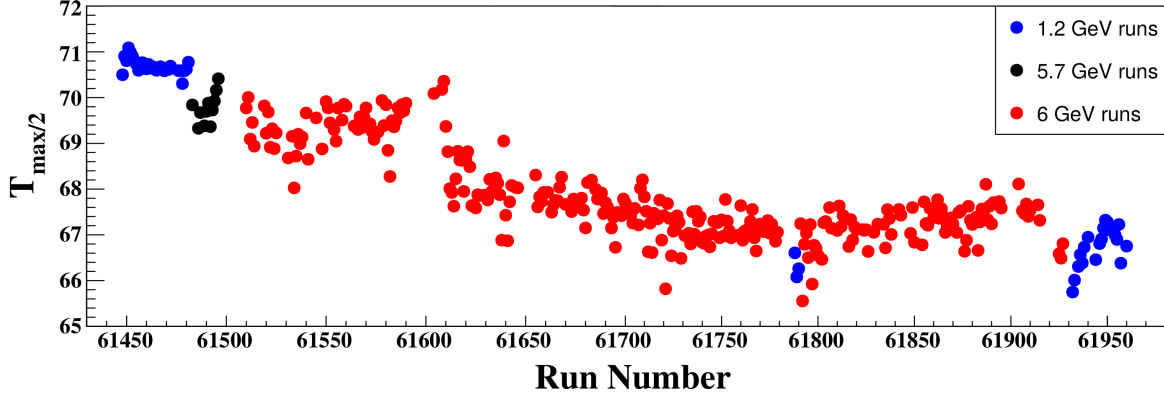


Figure 9:  $T_{max}/2$  versus the experimental run numbers.

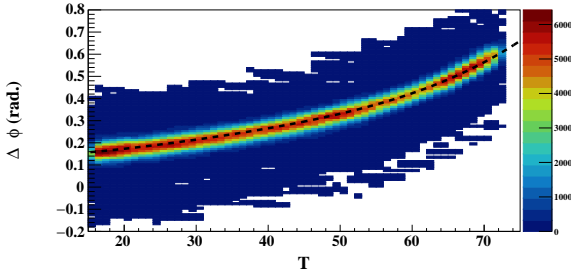


Figure 10:  $\Delta\phi$  versus  $T$  distribution for tracks from one bin in longitudinal position along the RTPC. The black line represents the final drift paths in this bin.

limum nucleus. By comparing the calculated momentum and angle of the recoil alpha particle to the measurement in the RTPC, we tuned the drift paths independently of our knowledge of the chamber's conditions.

Based on the kinematics of the electrons in the calibration data, we generated the Helium nucleus in our GEANT4 simulation [17]. Then, we compared the calculated GEANT4 trajectory of the Helium nuclei to the hits measured in the chamber. To perform this drift path extraction, we made a first approximation assuming a linear dependence between the radius of emission of the charge and its time of detection, and then refined our result. Indeed, because of the magnetic field, the drift paths are not linear in the RTPC, but the curvature was minimal and this process converged already on the second iteration.

At the end of the extraction procedure, the azimuthal difference between the detection pad and the ionization point ( $\Delta\phi$ ) was extracted as a function of time. In Figure 10, we show the resulting data points for one bin in z-coordinate of the RTPC, where the drift path is easily identified and eventually fitted for implementation in our reconstruction code.

To verify the stability of the drift paths, this procedure was carried out using both the 1.204 GeV data from the beginning of the run period and the 1.269 GeV data from

the end of the run period (shown in blue on Figure 9). Interestingly, we found very similar drift paths for the two data sets and concluded that any changes in the system only significantly affected the drift speed.

#### 4.3. Gain Calibration

To calibrate the gains, we compared the experimental ADCs to the energy deposited for each pad individually in GEANT4 by similar simulated tracks (using the same elastic events as for the drift paths calibration). This requires a very good GEANT4 simulation including drift paths and the spread of the charge along the path before reaching the pad, so that the simulated hits match the experimental ones. Moreover, the simulation has to match the DAQ features that can lead to cutting out some hits. After setting the simulation properly, we compared simulation to experiment on an event by event basis as shown in Figure 11. The gain for each pad was calculated as the ratio of the measured ADCs to the simulated deposited energy. Then, This set of the gains was applied to the experimental data. We noticed that some pads record lower ADCs than expected. For this reason, we wanted to make sure that the recorded ADCs by a given pad are similar to the ADCs recorded by other pads in the same track. At this step, we compared the mean ADCs of each pad to the mean ADCs of the whole track. This ratio is collected for each pad from a sample of elastic events and a gain correction factor is extracted and applied to the first extracted gain ratio giving a final gain for each readout pad. Final results are shown in Figure 12, where energy loss of particles is plotted against momentum over charge ratio. One can clearly see the band for  $^4\text{He}$  in its expected position.

## 5. Track Reconstruction

### 5.1. Noise Rejection

Two independent noise signatures were identified in the raw data and removed in software prior to track reconstruction. Both are transient and isolated to a subset of the readout channels.

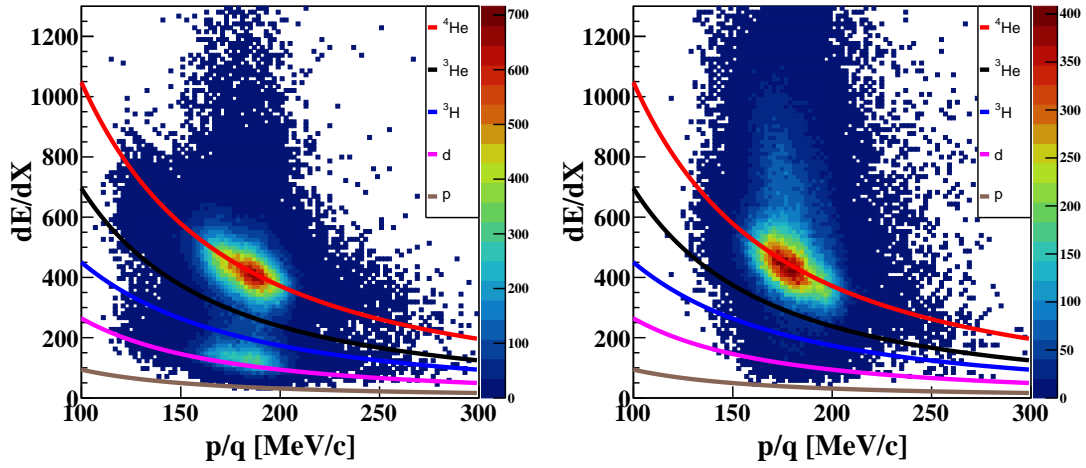


Figure 12:  $\frac{dE}{dX}$  vs.  $p/q$  distributions for the left (on the left) and for the right (on the right) half of the RTPC after gain calibration. The lines are theoretical expectations from the Bethe-Bloch formula for  $^4\text{He}$  (red),  $^3\text{He}$  (black),  $^3\text{H}$  (blue),  $^2\text{H}$  (pink) and protons (gray).

The first is an oscillatory noise located early in the readout time window, shown in the top panel of Figure 13 for a particularly noisy channel. Its amplitude is similar to those of real tracks. About 18% of the readout channels exhibit large contributions from this noise characteristic. Due to its unique time-energy correlation for the given channels, the noise could be removed on an event by event and channel by channel basis without significant loss of good signals. The result of the procedure is illustrated in the bottom panel of Figure 13.

The second noise signature was a coherent noise affecting about 25% of the pre-amplifiers boards, when simultaneous hits in most of the 16 channels of the board were recorded. An event-based technique to identify and remove this noise was developed based on counting simultaneous hits in each pre-amplifier group, and, if sufficiently large, perform a dynamic pedestal subtraction based on the average ADC of neighboring channels within this group.

The sources of these effects were not determined, but rejection techniques allowed to reconstruct 10% more good tracks and recover 70 channels that were previously ignored due to excessive noise levels.

## 5.2. Track Fitting

The tracking starts with reconstructing the spacial origin of the hits using the extracted drift speed and drift path parameters. For each registered hit, we calculate a position of emission from the signal time and the pad position. The third step is to create chains of hits. The maximum distance between two close adjacent hits has to be less than 10.5 mm to chain them, which roughly corresponds to neighbors and next to neighbors. We fit the chains with a helix if they have a minimum of 10 hits. We then eliminate from the chain the hits that are 5 mm or farther from the fit, as they are not likely part of the same

track. This new reduced chain is used for a second and final helix fit.

For energy deposition, the mean  $\frac{dE}{dx}$  is calculated as

$$\left\langle \frac{dE}{dX} \right\rangle = \frac{\sum_i \frac{ADC_i}{G_i}}{L}, \quad (1)$$

where the sum runs over all the hits of the track,  $G_i$  is the gain of the associated pad, and  $L$  is the visible track length in the active drift volume.

## 5.3. Energy Loss Corrections

Energy loss between the target and drift region was significant in the RTPC and necessitated a correction for optimal momentum reconstruction at the primary interaction vertex. The dominant loss was in the 27  $\mu\text{m}$  thick Kapton target wall, with significant contributions also from the pressurized target gas and the foils before reaching the drift region. Corrections were developed based on GEANT4 simulations with the full RTPC geometry and parameterized in terms of recoil curvature in the drift region and polar angle, separately for all recoil hypotheses ( $p$ ,  $d$ ,  $^3\text{H}$ ,  $^3\text{He}$ ,  $^4\text{He}$ ). At our average coherent  $^4\text{He}$  DVCS kinematics, energy losses were about 5 MeV, while for  $e-^4\text{He}$  elastic scattering losses were about 3 MeV, which corresponds to momentum corrections of 25% and 15%, respectively.

## 6. Performance Studies

The primary data sample used for calibration and performance assessment of the RTPC was elastic scattering with a 1.2 GeV electron beam. The electron momentum and direction is measured with CLAS, which uniquely determines the expected recoiling  $^4\text{He}$  kinematics. Matching requirements between reconstructed and expected  $z$ -vertex

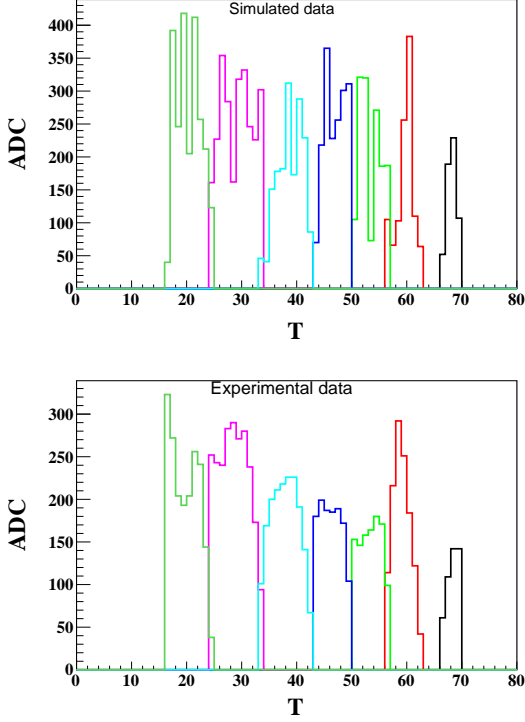


Figure 11: Simulated (upper) and experimental (lower) ADC and  $T_{26}$  distributions of a track. The colors indicate the pads, same color in top and bottom indicate that they are the same pad.

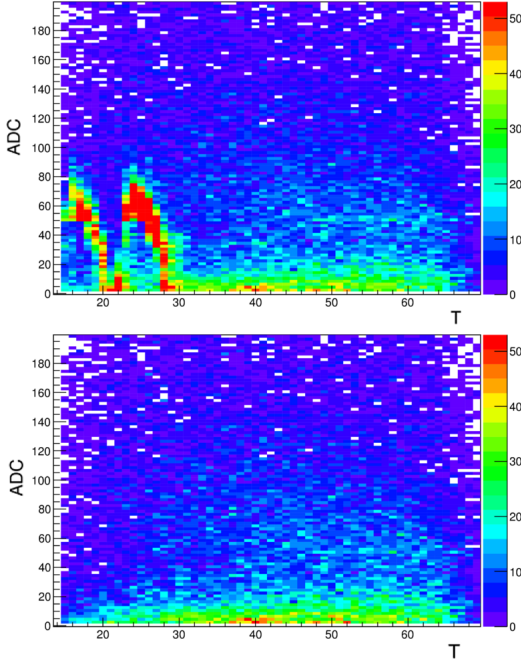


Figure 13: The ADC vs.  $T$  spectrum for an example noisy channel before (top) and after (bottom) noise rejection algorithms. Only hits associated with tracks are included, and the selection of events and tracks is the same in both plots.

and direction of the RTPC track provides a clean selection of elastically-scattered  $^4\text{He}$ , shown in Figure 14.

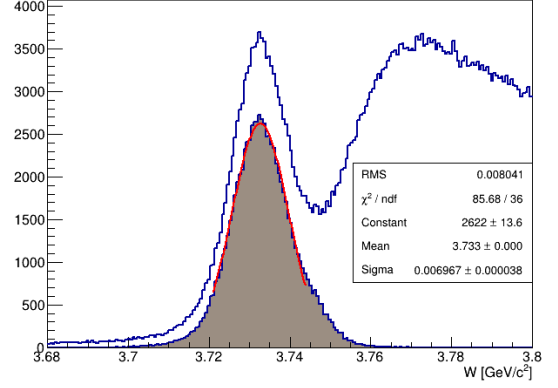


Figure 14: The recoil mass  $W$  distribution calculated from electron kinematics before (“inclusive”) and after (“exclusive”) requiring a matching track in the RTPC.

### 6.1. Resolution

Elastic scattering was used to estimate the tracking resolution of the RTPC based on the residual between the expected and measured  $^4\text{He}$  tracks. The RTPC resolutions, after removing contributions from the electron, are shown in Table 1, and are very similar for the two halves of the detector. Note that the  $\theta$ - and  $z$ -resolutions are highly correlated.

	$\sigma_z$	$\sigma_\theta$	$\sigma_\phi$	$\sigma_p/p$
Left	5.3 mm	3.8°	1.9°	9%
Right	6.5 mm	4.0°	1.9°	8%

Table 1: The resolutions of the two modules of the RTPC for  $z$ -vertex, polar and azimuthal angles, and momentum.

### 6.2. Efficiency

We measured the efficiency of the RTPC using elastic scattering on  $^4\text{He}$  by comparing the inclusive yield, based only on electron detection, to the exclusive elastic yield, where the Helium recoil is also detected (see Figure 14). We present in Figure 15 the results for the two halves of the detector. We observe that the left and the right modules have similar efficiencies except near the upstream target window. This difference is due to the large number of dead channels concentrated in this part of the left half of the detector

## 7. Conclusion

We reported on the construction, operation and calibration of a small RTPC designed to measure  $^4\text{He}$  nuclei in high rate environment. The operation of the detector was successful and allowed to detect Helium nuclei with a 75% efficiency and a readout rate of 3.1 kHz triggered by the detection of high energy electrons and photons in the CLAS spectrometer.



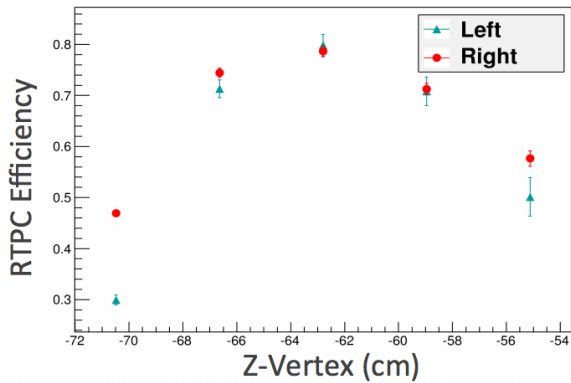


Figure 15: The RTPC  $^4\text{He}$  detection efficiency as a function of the longitudinal position along the detector.

## 8. Acknowledgments

The authors thank the staff of the Accelerator and Physics Divisions at the Thomas Jefferson National Accelerator Facility who made this work possible. This work was supported in part by the French Centre National de la Recherche Scientifique (CNRS), the Italian Istituto Nazionale di Fisica Nucleare (INFN) and the U.S. Department of Energy. M. Hattawy also acknowledges the support of the *Consulat Général de France à Jérusalem*. The Southeastern Universities Research Association operates the Thomas Jefferson National Accelerator Facility for the United States Department of Energy under contract DE-AC05-06OR23177. This material is based upon work supported by the U.S. Department of Energy, Office of Science, Office of Nuclear Physics, under contract number DE-AC02-06CH11357.

## References

- [1] B. A. Mecking *et al.* [CLAS Collaboration], The CEBAF Large Acceptance Spectrometer (CLAS), Nucl. Instrum. Meth. A **503**, 513 (2003).
- [2] M. D. Mestayer *et al.*, The CLAS drift chamber system, Nucl. Instrum. Meth. A **449**, 81 (2000).
- [3] G. Adams *et al.*, The CLAS Cherenkov detector, Nucl. Instrum. Meth. A **465**, 414 (2001).
- [4] E. S. Smith *et al.*, The time-of-flight system for CLAS, Nucl. Instrum. Meth. A **432**, 265 (1999).
- [5] M. Amarian *et al.*, The CLAS forward electromagnetic calorimeter, Nucl. Instrum. Meth. A **460**, 239 (2001).
- [6] F. X. Girod *et al.* [CLAS Collaboration], Measurement of Deeply virtual Compton scattering beam-spin asymmetries, Phys. Rev. Lett. **100**, 162002 (2008).
- [7] Hyon-Suk Jo, Etude de la Diffusion Compton Profondément Virtuelle Sur le Nucléon avec le Détecteur CLAS de Jefferson Lab: Mesure des Sections Efficaces polarisées et non polarisées, IPNO-Thesis (2007).
- [8] G. Asryan *et al.*, Meson spectroscopy in the Coherent Production on  $^4\text{He}$  with CLAS, Jlab proposal to PAC31 (2007).
- [9] K. Hafidi *et al.*, Deeply virtual Compton scattering off  $^4\text{He}$ , Jlab proposal to PAC33 (2008).
- [10] H. C. Fenker *et al.*, BoNuS: Development and Use of a Radial TPC using Cylindrical GEMs, Nucl. Instrum. Meth. A **592**, 273 (2008).
- [11] F. Sauli, The gas electron multiplier (GEM): Operating principles and applications, Nucl. Instrum. Meth. A **805**, 2 (2016).

- [12] S. Bachmann *et al.*, Performance of GEM detectors in high intensity particle beams, Nucl. Instrum. Meth. A **470**, 548 (2001).
- [13] S. F. Biagi, Monte Carlo simulation of electron drift and diffusion in counting gases under the influence of electric and magnetic fields, Nucl. Instrum. Meth. A **421**, no. 1-2, 234 (1999).
- [14] L. Musa *et al.*, The ALICE TPC front end Electronics Nuclear Science Symposium Conference Record, 2003 IEEE, 5 3647-3651 Vol.5, Oct (2003).
- [15] H. K. Soltveit *et al.*, The Preamplifier shaper for the ALICE TPC-Detector, Nucl. Instrum. Meth. A **676**, 106 (2012).
- [16] R. Esteve Bosch, A. Jimenez de Parga, B. Mota and L. Musa, The ALTRO chip: A 16-channel A/D converter and digital processor for gas detectors, IEEE Trans. Nucl. Sci. **50**, 2460 (2003).
- [17] <http://geant4.cern.ch>